The Partition of Finescale Energy into Internal Waves and Subinertial Motions

K. L. POLZIN

Woods Hole Oceanographic Institution, Woods Hole, Massachusetts

E. KUNZE

Applied Physics Laboratory, University of Washington, Seattle, Washington

J. M. TOOLE AND R. W. SCHMITT

Woods Hole Oceanographic Institution, Woods Hole, Massachusetts

(Manuscript received 23 January 2002, in final form 15 July 2002)

ABSTRACT

Finescale vertical wavenumber strain spectra (strain: normalized buoyancy frequency variability or vertical derivative of isopycnal displacement) are consistently less steep than shear spectra (shear: vertical derivative of horizontal velocity) for vertical wavelengths smaller than several tens of meters. Interpreting the diminished ratio of shear to strain (shear/strain ≡ horizontal kinetic/available potential energy) at higher vertical wavenumber as due to a greater contribution from high-frequency internal waves is not consistent with extant internal wave–wave interaction theories. A contribution from low-aspect-ratio subinertial density fine structure (flattened structures referred to herein as vortical modes) is therefore hypothesized. Vertical wavenumber spectra for vortical mode shear and strain are inferred from the observed spectra. Observed correlations between shear squared and buoyancy frequency squared exist that cannot be explained by either linear internal waves or geostrophic vortical modes. A model of internal wave–vortical mode interactions is used to interpret the observed correlations and partition the finescale spectra into internal wave and vortical mode components. A simple Doppler shift model is used with current meter data to refine the partitioning. The inferred vortical modes have an aspect ratio of approximately f/N (f: Coriolis frequency, N: buoyancy frequency), an rms velocity of 0.7 cm s^{-1}, and bandwidth-limited gradient spectra. At vertical wavelengths larger than 30 m the vortical modes are inferred to be quasi-geostrophic and in thermal wind balance. The data are interpreted as exhibiting an approximate equipartition between waves and vortical modes at vertical wavelengths smaller than 10 m.

1. Introduction

Three solutions to the linearized f-plane equations exist. Two of these solutions represent internal waves with $f < |\omega| < N$. The third solution is the geostrophic balance with intrinsic frequency $\omega = 0$. In the context of finescale dynamics, the third solution has been referred to as a vortical mode, irreversible or permanent fine structure, pancake eddies, blini, or geostrophic turbulence. It carries potential vorticity perturbations that can only be created or destroyed through irreversible processes. Internal waves are generally assumed to dominate velocity and density fluctuations on vertical scales smaller than a few hundred meters (e.g., Garrett and Munk 1979). However, vortical modes (Holloway 1983; Müller 1984) could also be present.

Interpreting finescale observations is further complicated by the presence of nonlinearity within the internal wavefield (i.e., Doppler shifting). Analyses of time series from moored arrays (Briscoe 1977; Müller et al. 1978) found need to invoke velocity fine structure (with amplitudes of 0.26 and 2 cm s^{-1}, respectively, and vertical wavelengths ≤10 m) to explain higher ratios of horizontal kinetic to available potential energy (HKE/APE) than predicted by linear theory within the internal wave continuum band ($f \ll \omega \ll N$). In float records, Kunze et al. (1990) found excess finescale APE at near-inertial frequencies as well as excess HKE at higher frequencies and argued that this result was consistent with Doppler shifting of finescale internal waves across frequency. This interpretation is consistent with Sherman and Pinkel (1991) finding an increasingly flat Eulerian frequency strain spectrum with increasing vertical wavenumber that, when transformed into an isopycnal (semi Lagrangian) coordinate system to account for vertical (but not horizontal) Doppler shifting, became red at all resolved vertical wavenumbers. Anderson (1992) reached similar conclusions with shear, finding remark-

Corresponding author address: Dr. K. L. Polzin, WHOI, MS 21 Woods Hole Road, Woods Hole, MA 02543.
E-mail: kpolzin@whoi.edu

able agreement with linear internal wave kinematics for frequencies $f < \omega \ll N$ at all but the highest-resolved wavenumber band (10–16 m), where horizontal advection may be responsible for the discrepancy. D'Asaro and Lien (2000) likewise find the buoyancy frequency cutoff ($\omega \cong N$) is much better defined in data from a Lagrangian float than in Eulerian measurements. These studies suggest that Eulerian measurements at these scales are contaminated by Doppler shifting and that finescale velocity and density fields are dominated by internal waves rather than vortical modes. In contrast, XCP surveys found significant vortical mode contributions at vertical wavelengths of 40 m (D'Asaro and Morehead 1991) and 50–400 m (Kunze 1993).

These two views of ocean fine structure are not necessarily incompatible. Both D'Asaro and Morehead (1991) and Kunze (1993) identify nearby topography as the likely source of their vortical mode signal. Anderson's (1992) data was from a site well removed from topography and may simply reflect a relative absence of vortical mode energy due to the lack of nearby sources. Low aspect ratio vortical modes, having more strain than shear, might also be transparent to Anderson's isopycnal analysis.

In this paper we attempt to quantify vortical mode amplitudes in vertical profile data. Section 2 briefly describes the instrumentation, datasets, and analysis techniques. Section 3 reviews the normal mode decomposition of the linearized f-plane equations. Observed vertical wavenumber spectra are presented in section 4. In section 5, the vortical mode strain spectrum is diagnosed with the use of a fine structure model for observed correlations between shear-squared S^2 and buoyancy-frequency-squared N^2. Current-meter data are examined and compared with the vertical profile data in section 6.

2. Data description

a. Instrumentation

The vertical profile data in this study were obtained with the High-Resolution Profiler (HRP), a free-falling, internally recording instrument (Schmitt et al. 1988). Relative velocities are measured with an acoustic velocimeter, with profiles of oceanic velocity computed from the relative velocity, accelerometer, and magnetometer data using a variation of the Total Ocean Profiling System (TOPS) point-mass model (Hayes et al. 1984). Temperature, conductivity, and pressure are sensed with an Neil Brown Instrument Systems Mark III CTD. The salinity calculation utilizes the Horne and Toole (1980) algorithm to correct for sensor response mismatch. The data are bin averaged over 0.5-dbar intervals.

b. Datasets

The data we present were obtained during four field experiments:

1) FASINEX (Frontal Air–Sea Interaction Experiment)

Field work took place in February–March of 1986 in the vicinity of an upper-ocean front in the subtropical convergence zone of the northwest Atlantic (29°N, 68°W) (Weller et al. 1991). The finescale velocity and density profiles revealed a complex pattern of variability associated with the frontal velocity structure in the upper 250 m. This pattern was interpreted in terms of internal wave–mean flow interactions by Polzin (1992). In this paper, segments of 29 profiles from depths of 250–860 m are examined.

2) WRINCL (Warm Ring Inertial Critical Layer)

The 40 WRINCL profiles examined here were obtained during March–April 1990 in a Gulf Stream warm-core ring (40°N, 64°W). Consistent with expectations for preferential generation (e.g., Rubenstein and Roberts 1986) and wave–mean flow interactions (Kunze 1985), the data exhibit heightened spectral levels and enhanced near-inertial energy, that is, elevated shear relative to strain. The ring's relative vorticity in the depth range 372–628 m used here was -0.05 to -0.15 times f. Background information and further analysis of these HRP data appear in Polzin et al. (1995), Kunze et al. (1995), and Polzin (1996).

3) TOPO (Fieberling Guyot)

These 13 profiles were taken 15–37 km from Fieberling Guyot in 3400–4500 m of water in the eastern North Pacific Ocean. The seamount is 1000 km west of Southern California (32°25′N, 127°47′W) in a region of water mass confluence outside the influence of the California Current (Roden 1991). Background currents were less than 2–3 cm s^{-1} (Brink 1995, his Fig. 13). Data from the depth interval 300–1050 m are examined here and include five additional profiles to those examined in Polzin et al. (1995) and Polzin (1996). Further background information and analysis can be found in Toole et al. (1997) and Kunze and Toole (1997).

4) NATRE (North Atlantic Tracer Release Experiment)

Data from NATRE will constitute the bulk of our analysis. These data were collected during April 1992 southwest of the Canary Islands (Fig. 1) as part of an initial site survey prior to injection of a tracer (Ledwell et al. 1998). The stations include 100 profiles on a 400 km × 400 km grid and 44 profiles near the center of the grid. At the depths of interest (see below) shear, strain, and dissipation were roughly homogeneous over the horizontal extent of the survey. Prior analyses of these HRP data appear in Polzin et al. (1995) and Polzin

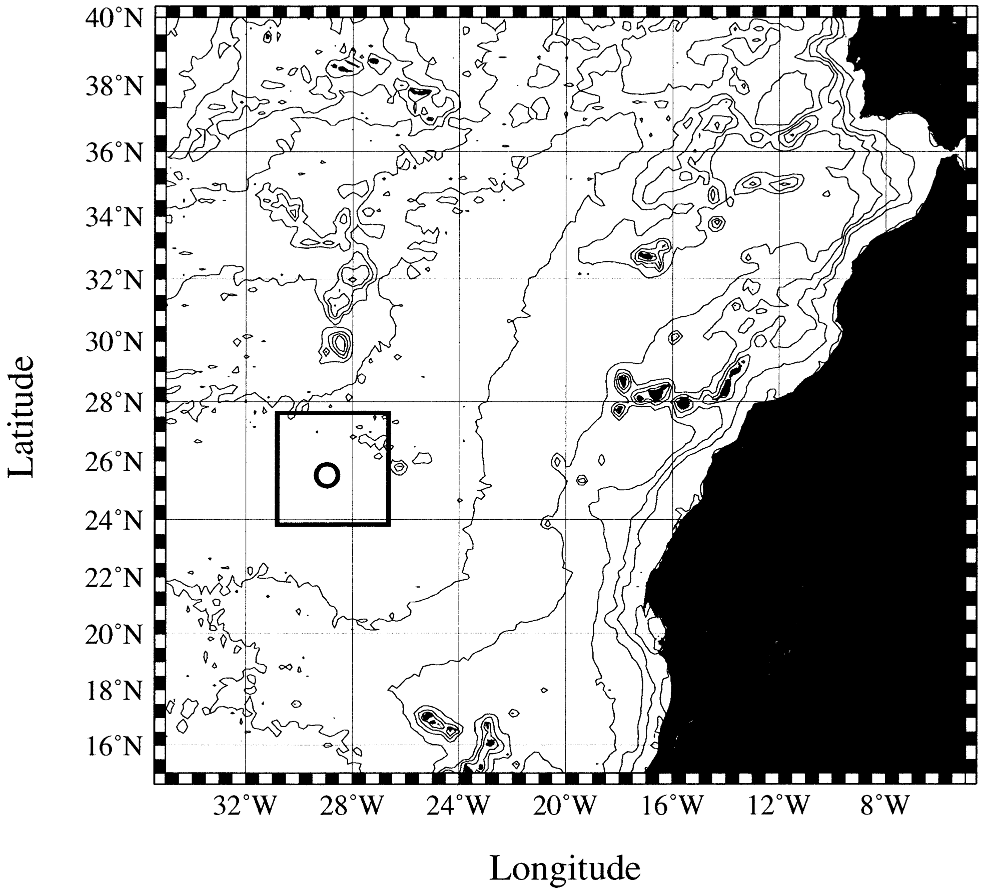

FIG. 1. Location of the HRP grid survey for the North Atlantic Tracer Release Experiment (NATRE). The grid survey is enclosed by the square centered about 26°N, 29°W. The open circle denotes the position of the current-meter mooring discussed in the text.

(1996). St. Laurent and Schmitt (1999) discuss estimates of vertical diffusivity derived from these data.

The NATRE data are analyzed over pressure ranges of 225–475 and 400–800 dbar. The shallower interval encompasses both the isopycnal nominally at 310 dbar on which the tracer was injected and the depths of current meters deployed on a mooring at the center of the survey. The deeper interval spans 600 dbar where the correction scheme to match the conductivity and temperature sensor response has its optimal response and exhibits smaller depth variability in $\overline{N^2}(z)$. The vertical wavenumber spectra of strain (N^2) are not contaminated by noise for vertical wavenumbers smaller than 0.4 cpm in the pressure range 400–800 dbar and 0.2 cpm higher in the water column. Data from the deeper interval are used to quantify the correlation between shear-squared and N^2 in section 5 in order to minimize possible effects of noise, minimize statistical inhomogeneity [$\overline{N^2}(z)$ varies by 20% over this deeper pressure interval while trends in $\overline{N^2}(z)$ are more than twice as large in the shallower interval], maximize the number of degrees of freedom and facilitate comparison with previous analyses. A spectral analysis of both depth intervals is presented for comparison purposes.

The HRP survey in NATRE was near the center of a moored array deployed as part of the subduction experiment (Weller et al. 2002, unpublished manuscript). Principal interest here is mooring C with a vector measuring current meter (VMCM) pair at 300 and 310 m. Data from the second deployment of that mooring (12 Feb–14 Oct 1992) are analyzed here.

c. Analysis techniques

This analysis focuses upon the interpretation of vertical profiles of horizontal velocity and density. Of particular interest is the relationship between shear-squared ($S^2 = U_z^2 + V_z^2$, where U_z and V_z are the vertical gradients of the horizontal velocity components) and a normalized version of N^2 variability $\eta_z = (N^2 - \overline{N^2})/\overline{N^2}$ commonly referred to as strain in the internal wave literature. Strain can be interpreted as a measure of the squashing and separation of isopycnals associated with the differential displacements by internal waves. Shear-squared and strain variance share a common interpretation as gradient versions of HKE and APE.

1) Spatial analysis

The correlation between N^2 and shear-squared is examined in section 5 using the NATRE data. Linear least squares fits in depth to vertical profiles of horizontal velocity were used to estimate S^2. Buoyancy frequency squared was estimated using the adiabatic leveling method (Bray and Fofonoff 1981), which utilizes a linear least squares fit to the specific volume anomaly profile. For this analysis, data were scaled with various estimates of the background buoyancy frequency squared, $\overline{N^2}^{xyt}$, to account for statistical inhomogeneity associated with depth $\overline{\text{variations}}^{xyt}$[1] in $\overline{N^2}^{xyt}$. The $\overline{N^2}^{xyt}$ profile was estimated by averaging temperature and salinity on pressure surfaces and utilizing a 100-m fit length. The buoyancy scaling of S^2 and N^2 follow from Wentzel–Kramers–Brillouin (WKB) scaling of spectral density and a constant fit length for vertical gradients. This scaling renders the NATRE dataset to be statistically homogeneous in the vertical (Polzin 1996).

2) Spectral analysis

Shear $[S_z(m)]$ and strain $[F_z(m)]$ spectra are presented in section 4. Profiles of vertical displacements were determined from the difference in pressure of constant potential density surfaces between individual and $\overline{\text{averaged}}^{xyt}$ profiles. Strain spectra were estimated as the product of vertical wavenumber squared and the displacement spectra. When shear and strain spectra are presented in the same figure, the shear spectra have been normalized by the average buoyancy frequency squared ($\overline{N^2}$).

3. Normal mode decomposition

As background for the interpretation of the data, a brief review of pertinent linear internal wave and vortical mode consistency relations (e.g., Lien and Müller 1992) is presented below. The primary result is that near-inertial internal waves have much larger horizontal than vertical scales and more HKE (and shear variance) than APE (and strain variance). For similar aspect ratios, the opposite (more APE than HKE) is true for vortical modes.

The linearized f-plane equations have three independent plane-wave solutions, that is, all variables proportional to $\exp\{[ikx + ly + mz - \omega t]\}$. For given wavevector (k, l, m), the corresponding frequencies (ω) satisfy

$$\omega_{\pm} = \pm\left(\frac{f^2m^2 + \overline{N^2}k_h^2}{m^2 + k_h^2}\right)^{1/2}, \qquad \omega_0 = 0, \tag{1}$$

where the horizontal wavenumber $k_h = (k^2 + l^2)^{1/2}$ and f is the Coriolis frequency. The ω_0 solution represents vortical modes in the low Rossby number (Ro) limit in which vertical shear is associated with horizontal density gradients through the thermal wind relation. In this limit, vortical modes are horizontally nondivergent and have an arbitrary vertical structure. Nonlinearity represents a small $[O \sim (\text{Ro}) \equiv u/fL = \zeta/f$, where u is a characteristic velocity with horizontal length scale L, and ζ is the relative vorticity$]$ perturbation to the thermal wind relation. The evolution of vortical modes over timescales $1/\zeta > 1/f$ is fundamentally nonlinear as the length scales are not sufficiently large for planetary wave propagation to be important. The $\omega_{\pm}$ solutions represent internal waves. In order for internal waves to propagate spatially, $f < |\omega_{\pm}| < \overline{N}$. In (1), the vertical wavenumber is assumed to be positive, implying internal wave frequencies of either sign. Upward (downward) phase propagation with downward (upward) energy propagation follows if $\omega > 0$ $(\omega < 0)$. The solutions ω_+ and ω_- therefore represent two distinct physical modes. Vortical modes have nonzero perturbation potential vorticity, whereas linear internal waves have none (Müller 1984).

The following relations can be derived from the f-plane equations.

For internal waves $(\omega_{\pm})$:

$$\frac{S_z(m)}{\overline{N}^2F_z(m)} = \frac{(\omega^2 + f^2)(\overline{N}^2 - \omega^2)}{(\omega^2 - f^2)\overline{N}^2} = \frac{\left(2 + B_r^2 + \dfrac{f^2}{N^2}B_r^2\right)}{B_r^2\left(1 + \dfrac{f^2}{N^2}B_r^2\right)} \tag{2}$$

For vortical modes (ω_0):

$$\frac{S_z(m)}{\overline{N}^2F_z(m)} = \left(\frac{\overline{N}k_h}{fm}\right)^2 \equiv B_r^2. \tag{3}$$

In (2) and (3), $S_z(m)$ is the shear and $F_z(m)$ the strain vertical wavenumber spectral density. The shear/strain ratio in (2) and (3) is identical to the ratio between horizontal kinetic and available potential energy. The shear/strain ratio for vortical modes (3) is the square of the Burger number B_r. Thus the Burger number represents a scaled aspect ratio and will be referred to as such. Available potential energy *dominates* the total energy of vortical modes at *low aspect ratios* (small B_r), whereas the *opposite is true* for internal waves. The limit $\text{Ro} \gg B_r^2$ (with $\text{Ro} \ll 1$) is termed geostrophic and

[1] Averages are denoted by an overbar. When the distinction is important, a following superscript denotes the coordinate being averaged over; x and y (horizontal coordinates), z (depth) and t (time). In practice, $\overline{\text{average}}^{xyt}$ represents a 400 km × 400 km × 25 day average dictated by the HRP sampling.

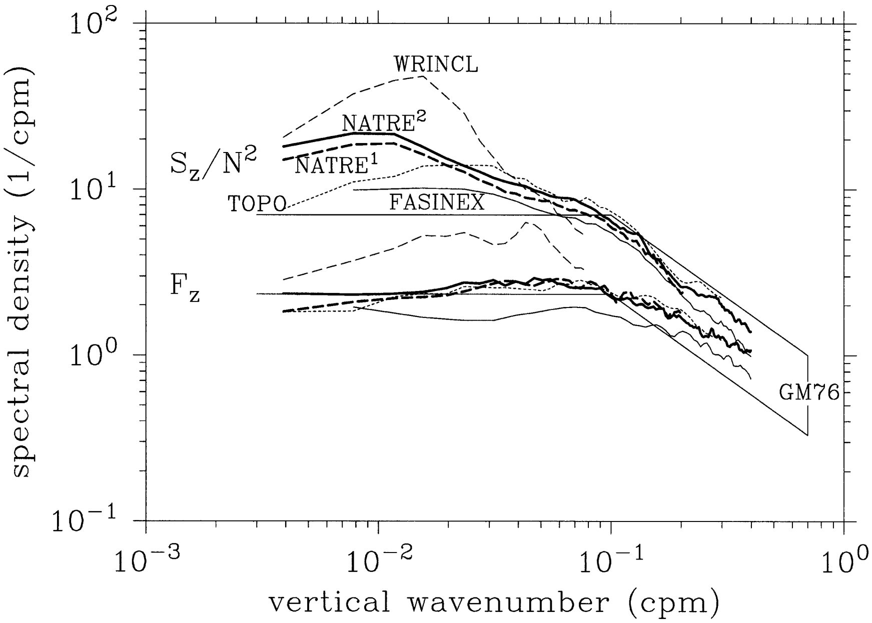

FIG. 2. Shear [$S_z(m)/\overline{N^2}$] and strain [$F_z(m)$] spectra for four midlatitude datasets [FASINEX (thin solid), NATRE[1] (thick dashed, 225–475 dbar), NATRE[2] (thick solid, 400–800 dbar), TOPO (dotted), and WRINCL (dashed)]. The thin straight lines denote the GM76 shear and strain spectra. Note that data from the two NATRE depth intervals are nearly identical.

$B_r^2 \gg$ Ro (Ro $\ll 1$) is quasigeostrophic. Quasi-permanent density fine structure, which has been viewed in the past as a passive, layered structure (e.g., Garrett and Munk 1971), is viewed here as having a finite horizontal extent and a dynamical interpretation as quasigeostrophic vortical modes.

The consistency relations (2)–(3) hold for plane-wave solutions to the linearized f-plane equations and thus represent an idealized situation. Nonlinearities in the vortical mode field alter the Burger number dependence of the shear/strain ratio (Kunze 1993). This effect is neglected here as are possible changes to the internal wave dispersion relation (1) associated with finite amplitude effects.

Vertical profiles are snapshots in time and thus integrate over all frequencies. Solving (2) for either B_r or ω allows one to assign a single characteristic frequency or aspect ratio to shear/strain ratios obtained in a broadband wavefield. However, the resulting estimates may not correspond to any particular moment of the frequency spectrum (Polzin et al. 1995). In particular, estimates of k_h/m derived from (2) tend to underestimate the sensitivity of the energy-weighted average

$$\overline{\frac{k_h}{m}} = \int_f^{\overline{N}} \left[\frac{(\omega^2 - f^2)}{(\overline{N}^2 - \omega^2)}\right]^{1/2} E(\omega)\, d\omega \Bigg/ \int_f^{\overline{N}} E(\omega)\, d\omega$$

to variations in $E(\omega)$, where $E(\omega)$ is the energy density frequency spectrum. The vertical profile data presented here likely consist of more than a single wave frequency, but the lack of frequency domain information prohibits us from pursuing such an interpretation.

4. Shear/strain ratio

Shear and strain spectra from our four midlatitude datasets exhibit a variety of low wavenumber amplitudes and spectral slopes (Fig. 2). At high wavenumber, however, the spectra are consistently red (pink?), with shear spectra falling off more steeply than strain. Consequently, for a given dataset, shear/strain ratios at high wavenumber are consistently smaller than at low wavenumber (Fig. 3). The shear/strain ratios exhibit a low wavenumber maximum, with values of 5–11 (Fig. 3b). Shear/strain ratios begin diminishing at wavenumbers lower than a cutoff value m_c typically taken as the transition to an m^{-1} spectral dependence.[2] At higher wavenumbers, shear/strain ratios asymptote to values between 1 and 2. In contrast, the Garrett–Munk model shear/strain ratio is 3.0, independent of vertical wavenumber. Recognition that decreasing shear/strain ratio with increasing wavenumber was a consistent signal in our data initiated this investigation.

The consistent character of the shear/strain ratio with

[2] On the basis of the GM76 spectral model (Garrett and Munk 1975, as modified by Cairns and Williams 1976) and a 0.1 cpm cutoff, Duda and Cox (1989) suggest the extended definition $\int_0^{m_c} S_z(m)\, dm = 0.7\overline{N^2}$. Here $m_c = 0.05$ cpm for the NATRE data.

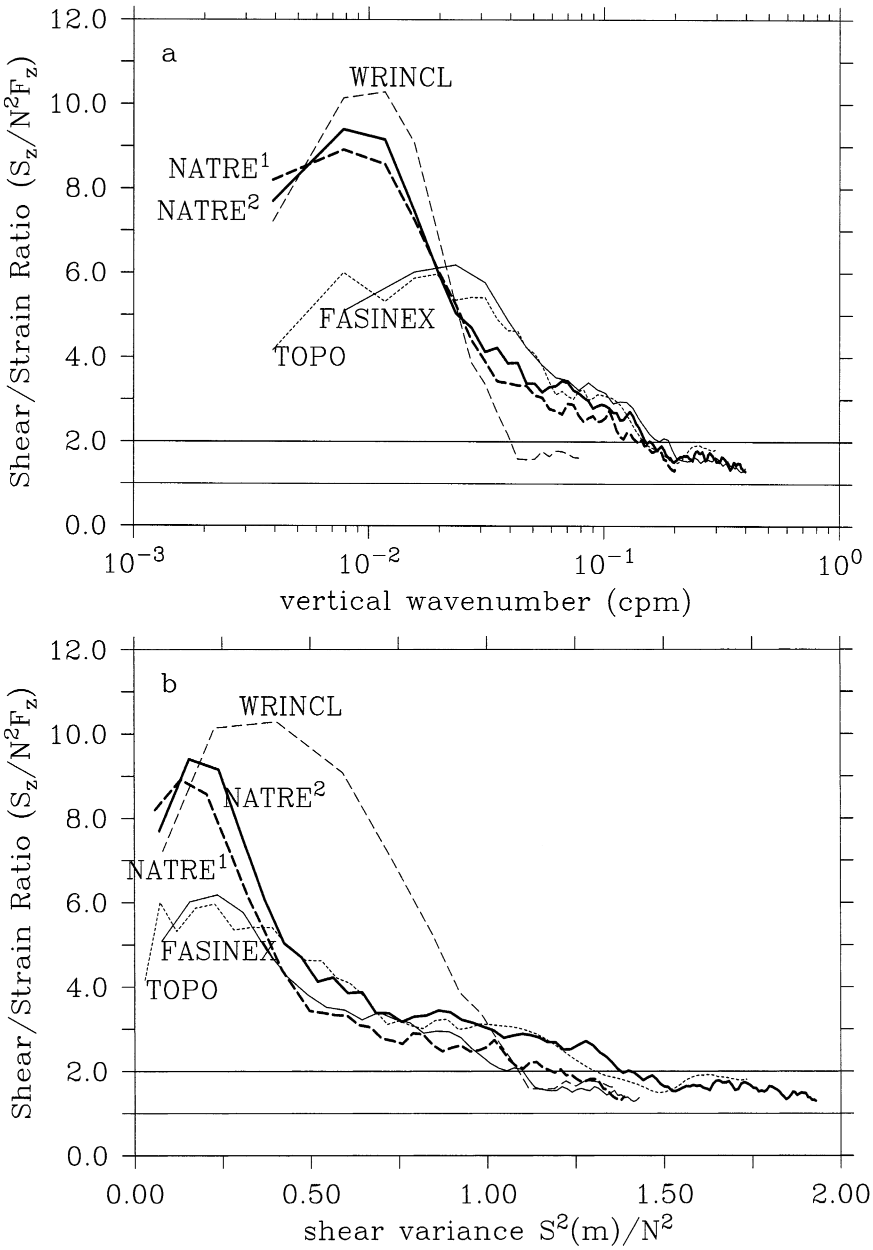

FIG. 3. Shear/strain ratios $[S_z(m)/\overline{N^2}F_z(m)]$ for the four midlatitude datasets in Fig. 2 as functions of both (a) vertical wavenumber and (b) cumulative shear variance, $\overline{S^2}(m)/\overline{N^2} = \int_0^m S_z(m)/\overline{N^2}\, dm$. The shear/strain ratio does *not* represent the cumulative variance. Rather, it is the ratio of the spectra. The choice of $\overline{S^2}(m)/\overline{N^2}$ as the ordinate axis in (b) represents an attempt to collapse some of the variability exhibited by the various datasets.

wavenumber suggests a common explanation. Possible causes for excess strain relative to shear include

- relatively more high-frequency internal waves at high vertical wavenumber [factor-of-3–4 higher aspect ratios and factor-of-2 higher frequencies at high wavenumber are implied by solving (2) with the observed shear/strain ratios],
- the presence of shear instabilities (e.g., Kelvin–Helmoltz billows) characterized by low shear/strain ratios, and
- increased finescale vortical mode variance at small scales.

Explaining the trend with wavenumber of the shear/strain ratio solely in terms of internal waves requires the local production of small-scale fluctuations. These high wavenumber internal waves have group velocities that are too small to expect that they propagate in from boundary sources. Internal waves propagate over distances equal to their vertical wavelength in a time $2\pi\omega/(\omega^2 - f^2)$. For frequencies characteristic of the GM spectrum [$f\sqrt{2}$, which can be obtained from (2) using the GM specification $S_z(m)/\overline{N^2}F_z(m) = 3$], this propagation timescale is approximately equal to the time required to dissipate the energy in the GM spectrum with vertical wavelengths smaller than 20 m. This latter timescale is estimated by integrating the GM energy spectrum over vertical wavelengths smaller than 20 m and dividing by the dissipation rate ascertained for the GM spectrum, 7×10^{-10} W kg^{-1} for $\overline{N} = 3$ cph (Polzin et al. 1995).[3]

The trend with wavenumber of the shear/strain ratio is, however, inconsistent with extant wave/wave interaction theories. Resonant interactions (McComas and Bretherton 1977) are dominated by the parametric subharmonic instability and induced diffusion mechanisms: both produce net spectral energy transfer to lower, not higher, frequencies. This result is confirmed by numerical simulations containing all interacting triads (McComas and Müller 1981). The eikonal (ray tracing) approach (Henyey et al. 1986) indicates upwavenumber, upfrequency spectral transfers for vertical wavenumbers such that

$$\overline{S^2}(m) \equiv \int_0^m S_z(m)\, dm < 0.25\overline{N^2}.$$

But at higher wavenumbers the predicted spectral flux results in substantially smaller changes in frequency. Our observations suggest an increase in the shear/strain ratio for $\overline{S^2}(m) < 0.25\overline{N^2}$, and then an abrupt decrease at higher wavenumber (Fig. 3b). Therefore, neither wave–wave interaction model appears to support an abrupt increase in wave frequency at the wavenumbers for which the abrupt decrease in the shear-to-strain ratio occurs. Note, however, that neither model is formally valid at $m \cong m_c$ (e.g., Polzin 2002, manuscript submitted to *J. Phys. Oceanogr.*).

Shear instability can produce high-frequency motions locally. However, unstable events [Ri $= N^2/S^2 < 1/4$; Miles (1961) and Howard (1961)] are not thick enough to explain the decreasing shear/strain ratio. In the NATRE data, only 3% of the water column is observed to have Ri $< 1/4$ at $\overline{S^2} = 1.0\overline{N^2}$ (Polzin 1996). This corresponds to a vertical scale smaller than the scale at which the shear/strain ratio begins to decrease (Fig. 3b). While shear instability acts to create high-frequency motions, it is unlikely to do so over sufficiently large vertical scales to explain our high wavenumber shear/strain ratios.

[3] These comments regarding the GM spectrum are also applicable to the observations despite differences in spectral levels, frequency content, and dissipation. For the NATRE experiment, [f, N, m_c, ϵ] = [6.4×10^{-5} s^{-1}, 1.35×10^{-5} s^{-2}, 0.05 cpm, 4.5×10^{-10} W kg^{-1}].

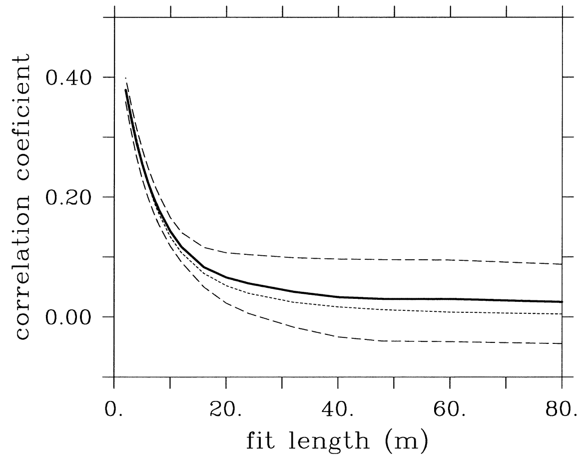

FIG. 4. Estimates of the S^2–N^2 correlation (7) as a function of fit length, Δz. Thick lines represent data from 400–800 dbar. Dashed lines represent the rms variability in correlation coefficients that were estimated by dividing the data into 50-m depth bins. The dotted line is a theoretical estimate using the parametric representation of the vortical mode spectrum (9) with the fine structure model (6–8) to estimate a correlation coefficient.

We hypothesize that the decreased shear/strain ratio at small vertical scales is due to vortical mode fine structure having a relative excess of strain, that is, structures with aspect ratios B_{r0} smaller than our average $\sqrt{S_z(m)/\overline{N^2}F_z(m)}$ estimates. A partitioning of energy between internal waves and vortical modes is attempted using a correlation analysis in section 5 and refined with the use of current meter data in section 6.

5. Correlation analysis

The NATRE data were used by Polzin (1996) to demonstrate that S^2 and N^2 are positively correlated. The S^2–N^2 correlation is an obvious feature in individual profiles [see Polzin (1996) for examples]. The correlation coefficient is small (0.03) at large vertical scales (80 m) but increases to significantly larger values (0.38) at vertical scales of 2 m (Fig. 4). Linear internal waves in constant background stratification do not give rise to such a correlation. The plane-wave vortical mode solution also gives zero correlation.

A correlation between S^2 and N^2 could arise from

- statistical inhomogeneity,
- vertical advection,
- turbulent momentum and buoyancy fluxes,
- response of internal waves to quasi-permanent density fine structure,
- straining of near-inertial shear by high-frequency strain (Kunze et al. 1990), or
- phase locking due to nonlinear wave–wave interactions (Desaubies and Smith 1982).

A WKB analysis reveals how the amplitude of internal waves varies with gradients in the background stratification. Larger shear variance and N^2 variability will be associated with larger background $\overline{N^2}^t$. Failure to scale observations acquired in a region with variable background $\overline{N^2}^t$ will result in a statistically inhomogeneous dataset that exhibits a nonzero correlation between S^2 and N^2 (first bullet). Scaling the NATRE data with the survey-averaged $\overline{N^2}^{xyt}$ results in a statistically homogeneous dataset, but does not eliminate the N^2–S^2 correlation (Polzin 1996). Buoyancy scaling can fail for a number of reasons. One of these occurs if internal-wave isopycnal displacements are larger than the scale of variation in $\overline{N^2}^t$ (second bullet). The N^2–S^2 correlation due to this effect in the NATRE data is small (Polzin 1996) as the trends in $\overline{N^2}^{xyt}$ over 400–800 db are small. Turbulent fluxes (third bullet) associated with shear instability cause a local reduction of shear and stratification and correlated N^2–S^2 anomalies (Polzin 1996). The reduction in shear is only temporary, with shear increasing to ambient values as small-scale waves propagate through the formerly unstable region and decrease the correlation resulting from the turbulent fluxes. In contrast, the reduction of background stratification in that region persists for much larger time periods and may give rise to a N^2–S^2 correlation if the amplitude of the small-scale waves is modulated by the resulting variability in the background stratification. To explore this further, a finestructure model was introduced with the purpose of examining the correlation produced by the interaction between internal waves and quasi-permanent density finestructure (fourth bullet). We subsequently use this model to estimate the amplitude of the vortical mode spectrum. A statistical model of the correlation resulting from the straining of near-inertial shear by higher-frequency strain (fifth bullet) is assessed in the appendix. Estimating the correlation arising from phase locking between internal waves (sixth bullet) is beyond the scope of this manuscript.

Internal waves are assumed to obey WKB scaling as they propagate in regions of spatially varying time/mean stratification, $\overline{N^2}^t$. In a broadband wavefield, WKB scaling and a fixed fit length imply the observed shear-squared, S^2_*, and buoyancy-frequency-squared, N^2_*, obey

$$N^2_* = (1 - \hat{\eta}_{z\pm})\overline{N^2}^t \qquad S^2_* = \hat{S}^2_\pm \overline{N^2}^t, \tag{4}$$

where $\hat{S}^2_\pm$ and $\hat{\eta}_{z\pm}$ are uncorrelated nondimensional stochastic variables representing the internal wavefield that are also uncorrelated with the time/mean stratification. Similarly, $\hat{S}^2_0$ and $\hat{\eta}_{z0}$ are nondimensional stochastic variables used to represent vortical modes.

The NATRE time-mean stratification profile, $\overline{N^2}^t$, is necessarily estimated here as a mixed spatial/temporal average, $\overline{N^2}^{xyt}$ (see footnote 1), over the horizontal domain (400 km × 400 km) of the survey. Vertical structure of the time-mean stratification that varies over the survey is therefore *not accounted for* in this implementation of the normalization scheme [(4) with $\overline{N^2}^t$ replaced by $\overline{N^2}^{xyt}$]. Potential sources of such anomalies include large-scale density gradients associated with the general circulation, baroclinic planetary waves, eddies, submesoscale coherent vortices, thermohaline intrusions, and vortical modes.

The key to quantitatively documenting the vortical mode spectrum is the recognition that the observed N^2–S^2 correlation can be understood as an incomplete accounting of the effects of WKB scaling, in particular those that result from spatial (x, y) variability in the time-mean stratification. The local, true time-mean stratification in (4),

$$\overline{N^2}^t = \overline{N^2}^{xyt} + \overline{\mathcal{N}^2}^{zt} + \overline{\mathcal{N}^2}^t, \tag{5}$$

consists of three parts:

1) a survey average profile $\overline{N^2}^{xyt}(z)$,
2) depth-independent spatially varying anomalies with zero horizontal average, estimated as $\overline{\mathcal{N}^2}^{zt} = \overline{N^2_i}^{zt} - \overline{N^2}$, where $\overline{N^2_i}^{zt}$ is an individual profile, depth average of N^2_* (over 400–800 dbar in the present case) and $\overline{N^2}$ is the depth average (again 400–800 dbar) of $\overline{N^2}^{xyt}$, and
3) a local depth-dependent contribution ($\overline{\mathcal{N}^2}^t$) that has zero horizontal and vertical average.

The $\overline{\mathcal{N}^2}^t$ component includes the vortical mode. Our NATRE estimates of $\overline{\mathcal{N}^2}^{zt}$ exhibit a large-scale spatial trend which appears to be associated with the structure of the subtropical gyre. A vertical scale separation dis tinguishes $\overline{\mathcal{N}^2}^t$ from $\overline{\mathcal{N}^2}^{zt}$. The scripted font $\mathcal{N}$ is used to intentionally delineate these contributions having zero horizontal average.

The observations consist in general of both wave and vortical contributions. The observations are represented here as

$$\begin{aligned} N^2_* &= (1 - \hat{\eta}_{z\pm})\overline{N^2}^t \\ S^2_* &= \hat{S}^2_\pm \overline{N^2}^t + \hat{S}^2_0(\overline{N^2}^{xyt} + \overline{\mathcal{N}^2}^{zt}), \end{aligned} \tag{6}$$

in which $\hat{S}^2_0$ represents the vortical mode shear, $\hat{S}^2_\pm$ the internal wave shear, $\hat{\eta}_{z\pm}$ the wave strain, and $\hat{\eta}_{z0} = [\overline{\mathcal{N}^2}^t - (\overline{N^2}^{xyt} + \overline{\mathcal{N}^2}^{zt})]/(\overline{N^2}^{xyt} + \overline{\mathcal{N}^2}^{zt})$ is the vortical mode strain. Zero interaction between internal wave shear and vortical mode shear has been assumed. This assumption is reconsidered in the discussion. The variables are normalized:

$$N'^2 = N^2_* \frac{\overline{N^2}}{\overline{N^2}^{xyt} + \overline{\mathcal{N}^2}^{zt}}$$

and

$$S'^2 = S^2_* \frac{\overline{N^2}}{\overline{N^2}^{xyt} + \overline{\mathcal{N}^2}^{zt}}$$

so that

$$\frac{\overline{N'^2 N'^2} - \overline{N'^2}^2}{\overline{N'^2}^2} = \hat{\eta}^2_{z\pm} + \hat{\eta}^2_{z0} + \hat{\eta}^2_{z\pm}\hat{\eta}^2_{z0}$$

$$\overline{S'^2} = \hat{S}^2_\pm \overline{N^2}^t + \hat{S}^2_0 \overline{N^2}^t,$$

and the correlation in Fig. 4 is estimated as

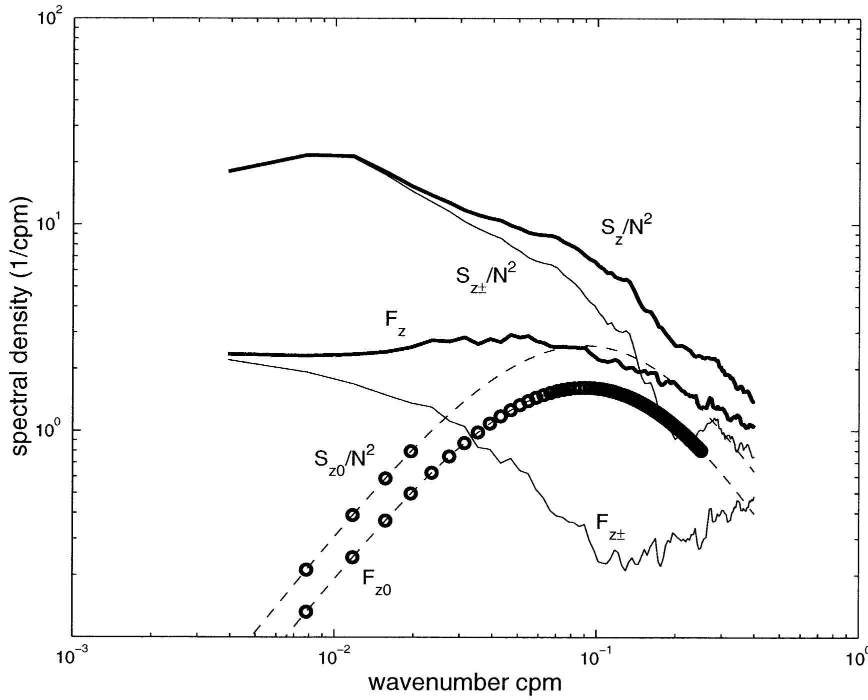

FIG. 5. Observed shear ($S_z/\overline{N^2}$) and strain (F_z) spectra for the NATRE dataset (400–800 dbar). Subscripts of ($\pm$) and (0) denote a decomposition into internal waves and vortical modes. The vortical mode spectra are delimited by circles where the parametric representation (9) is ground truthed by either the correlation analysis or the current-meter data.

$$C(\Delta z) = \frac{\overline{S'^2N'^2} - \overline{S'^2}\,\overline{N'^2}}{(\overline{S'^4} - \overline{S'^2}^2)^{1/2}(\overline{N'^4} - \overline{N'^2}^2)^{1/2}}. \qquad (7)$$

The correlation that arises from internal wave buoyancy scaling associated with quasi-permanent density fine structure in the time/mean stratification profile, which is not represented in the survey-averaged stratification profile, is simply

$$C(\Delta z) = \frac{\hat{\eta}^2_{z0}}{\overline{S'^2}^{-1}\overline{N^2}^{-1}(\overline{S'^4} - \overline{S'^2}^2)^{1/2}(\overline{N'^4} - \overline{N'^2}^2)^{1/2}}, \qquad (8)$$

where the numerator represents the vortical mode strain variance. The contribution of vortical modes to this correlation can be obtained by integrating the vortical mode strain spectrum [$F_{z0}(m)$]:

$$\hat{\eta}^2_{z0} = \int_{0.001\ \mathrm{cpm}}^{\infty} H(m, \Delta z)F_{z0}(m)\, dm,$$

where $H(m, \Delta z)$ is a transfer function which accounts for the filtering effect of a least squares fit of length Δz.

Various attempts to define F_{z0} from (8) were made, including solving (8) by iterative procedures. We found that the observed N^2–S^2 correlation could be predicted much more easily by employing a parametric representation of F_{z0} in the form of

$$F_{z0} = \frac{Am_2^2 m^r}{(m_1^r + m^r)(m_2^2 + m^2)}. \qquad (9)$$

This parametric spectral form (Fig. 5) prescribes a power-law behavior of m^r at low wavenumber, is white at intermediate wavenumbers and rolls off at high wavenumbers. Quite good agreement with the observed correlations are obtained with $A = 3.15$, $r = 2.0$, $m_1 = 0.055$, and $m_2 = 0.155$ (Fig. 4). The value of r is not well constrained by the finestructure model due to the lack of statistical reliability of the correlation estimates at large fit lengths. The constant r is determined by use of a simple Doppler shift model and current meter data discussed in the following section. The asymptotic limit at high wavenumber (m^{-2}) is not approached with the data at hand. The low-wavenumber transition from m^r to white is approximately m_c.

A simple interpretation of (8) is provided by noting the factor $(\overline{S'^4} - \overline{S'^2}^2)^{1/2}/\overline{S'^2}$ is observed to be within 10% of 1.0, which follows if S' is normally distributed. If the vortical mode contribution ($\overline{\eta^2_{z0}}$) to the total strain variance ($\overline{\eta^2_z}$) is small, (8) can be expressed as the product of the rms strain and the ratio between the vortical mode and total strain variances: $C(\Delta z)/\overline{\eta^2_z}^{1/2} \cong \overline{\eta^2_{z0}}/\overline{\eta^2_z}$. For fit lengths $40 < \Delta z < 80$ m, the rms strain is $0.1 < \overline{\eta^2_z}^{1/2} < 0.2$. The product of the observed correlation and the rms internal wave strain suggests the low wavenumber vortical mode strain variance is about 20% of the total. The near-zero correlation values at large fit lengths reinforce a bandwidth limited interpretation of the vortical mode spectrum.

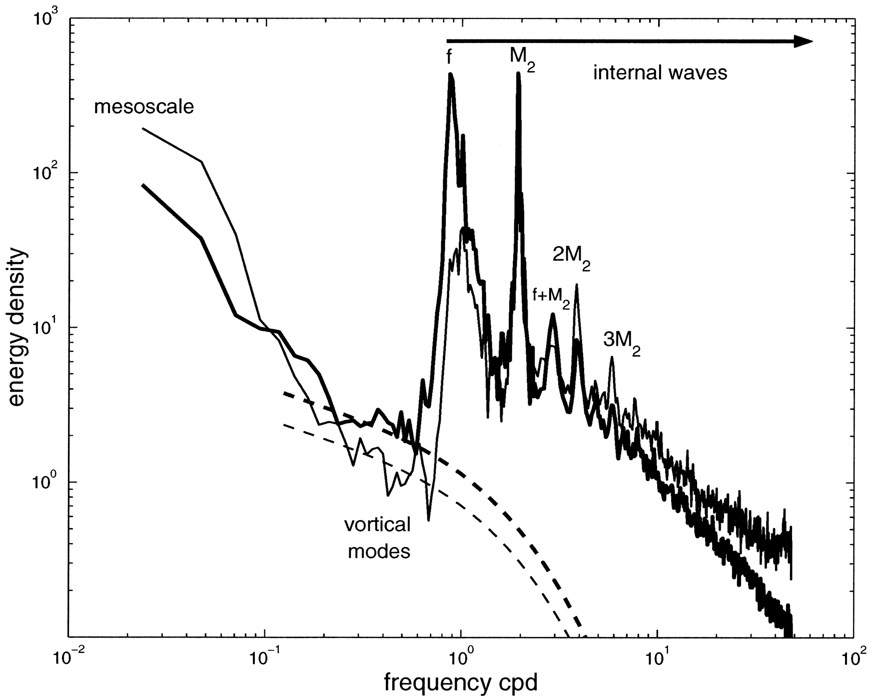

FIG. 6. Velocity (thick) and displacement (thin) frequency spectra for current-meter data (solid lines) at 300 m. Overplotted are the vortical mode energy spectra (dashed), converted to frequency spectra using a frozen fine structure model (10). For this model, 1 cpd corresponds to about 33-m vertical wavelength.

6. Current-meter data

A pair of closely spaced (10 m) current meters (VMCMs) were deployed on the center mooring of the subduction moored array in order to document the climatology of shear during the NATRE. These current-meter data exhibit features typical of midocean data: a red subinertial spectrum, and peaks at f, M_2, and several harmonics (Fig. 6). The continuum power-law behavior is slightly less steep than ω^{-2} (though note the records are not fully resolved in the temporal domain, as the sampling interval $\Delta t = 15$ min is larger than $\pi/N = 12.3$ min). Internal waves (superinertial frequencies) make a dominant contribution (≅80%) to the total horizontal kinetic energy (Table 1). In terms of the HKE/APE diagnostic (2), the superinertial horizontal velocity and displacement (η) statistics (inferred here as $T' = T - \overline{T}^t \equiv \eta \overline{T}^t_z$) are largely consistent with a linear internal wave interpretation (Fig. 7). However, by this diagnostic there is a 30% excess of APE in the continuum ($f^2 \ll \omega^2 \ll N^2$). This excess can be interpreted as fine structure contamination. This interpretation becomes more obvious when the coherence between the instruments is examined (Fig. 8). The disparity between velocity and temperature coherences at a given frequency indicates that the field is inconsistent with linear internal waves. The decreasing coherence with frequency is inconsistent with a vertical bandwidth independent of frequency (as in the GM models). These results are typical [see Müller et al. (1978) for a discussion and further references].

TABLE 1. Statistics of horizontal velocity and vertical displacement from VMCMs at 300 and 310 m near the center of the NATRE HRP grid. The velocity statistics are estimated from both north v and east currents u as $(u^2 + v^2)^{1/2}$, displacement statistics are estimated as $N(\overline{T'^2}/\overline{T}_z^2)^{1/2}$ with $N = 4.26 \times 10^{-3}$ s^{-1} estimated from the HRP grid survey and $\overline{T}_z = 1.89 \times 10^{-2}$ °C m^{-1} estimated at the time/mean temperature difference. The superinertial and bandpassed ($0.211 < w < 0.586$ cpd) statistics were made using Fourier transform methods. The subinertial statistics used a 2-day low-pass filter to isolate the subinertial components of the demeaned time series.

Frequency band	Subinertial	Bandpassed	Superinertial
Velocity (cm s^{-1})	2.22	0.42	4.82
N*Displacement (cm s^{-1})	3.20	0.33	3.79

Considerable effort has been expended trying to interpret such decreasing coherence as a finestructure contamination. Previous quasi-permanent finestructure models assumed 1) a specific vertical wavenumber spectral representation (steplike quasi-permanent finestructure profiles) and 2) that internal waves dominate at low wavenumber. These models interpret the increasing degradation of frequency domain coherence with increasing frequency in moored temperature data as representing the vertical advection of quasi-permanent density finestructure by internal waves. Several similar attempts were made with current-meter data (Müller et al. 1978;

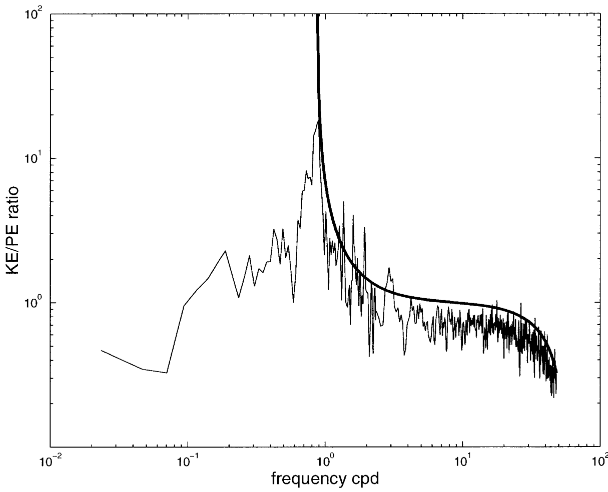

FIG. 7. HKE/APE ratio for the current-meter data in Fig. 6. The thick line represents (2). The observed ratio falls below the internal-wave prediction by ~30% for frequencies $1 < \omega < 40$ cpd.

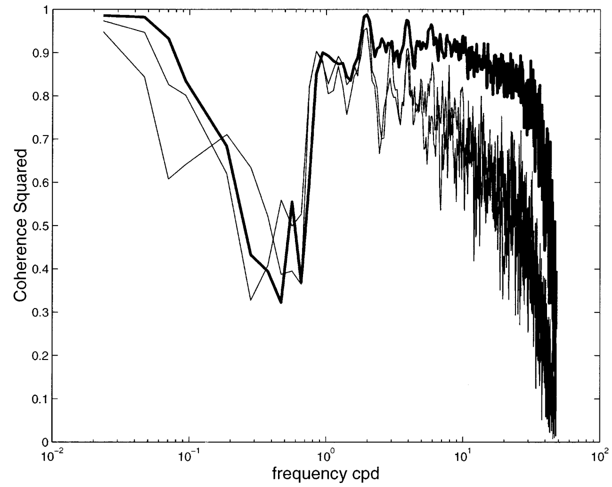

FIG. 8. Coherence records between two current meters at 300 and 310 m. Temperature (thick), north and east (thin).

Eriksen 1978; Briscoe 1977). These models share a common perspective of passive steplike velocity fine structure being vertically advected past spatially fixed sensors by internal waves. In contrast, Sherman and Pinkel (1991) and Anderson (1992) use time series of vertical profile data to interpret the fine structure contamination as an artifact of large, vertical-scale internal waves vertically advecting small, vertical-scale internal waves past an Eulerian sensor.

Both interpretations may be true in part, but neither addresses the correlation between N^2 and S^2. Our model (4)–(8) interprets the correlation as a response of internal wave shear to quasi-permanent density fine structure. It is most closely related to a suggestion by Garrett and Munk (1971) attempting to quantify the response of internal wave shear to steplike quasi-permanent density fine structure. Our model differs in that we use the correlation to solve for the vertical wavenumber structure of the quasi-permanent density finestructure field. We will further pursue a different tack by diagnosing quasi-permanent fine structure in the subinertial portion of the current-meter records rather than trying to sort out the fine structure contamination in the superinertial records.

Extracting information about the amplitude and aspect ratio of finescale vortical modes from the subinertial fields is problematic because the subinertial velocity and displacement fields are dominated by low mode contributions (i.e., the mesoscale eddy field). A modal decomposition of subinertial velocity records near the grid survey (Wunsch 1997) returns the result that 60%–70% of the depth-integrated subinertial kinetic energy is contained in the barotropic and first two baroclinic modes. The 10-m velocity and temperature coherences are quite high for periods longer than two weeks (Fig. 8) with HKE/APE ratios smaller than 1 (Fig. 7), which we take as being indicative of low-mode, low-aspect-ratio ($B_r < 1$) motions. At higher frequencies, the coherences are lower and the data are increasingly likely to reflect Doppler shifted vortical modes. Taking the bandwidth of $0.211 < \omega < 0.586$ cpd as being dominated by finescale vortical modes, one estimate of the vortical mode kinetic energy is $(u^2 + v^2)^{1/2} = 0.42$ cm s^{-1} with an HKE/APE ratio of 1.6 (Table 1).

This frequency band does not include higher (Eulerian) frequency contributions, which could be substantial. Small-scale vortical modes could be horizontally advected past the sensors at higher frequencies. In the limit of a frozen finestructure field in a time-independent flow field with velocity U, vortical modes with vertical wavenumber $m = \overline{N}k_h/fB_{r0}$ (3) will be swept past an Eulerian sensor at an apparent frequency $\sigma = kU \cong fmB_{r0}U/\overline{N}$. At a constant horizontal Doppler shift velocity of $U = 2$ cm s^{-1}, 10-m vertical wavelength vortical modes would have an apparent frequency of $\sigma \cong 3.3$ cpd. The bandwidth $0.211 < \omega < 0.589$ cpd, which is associated with $(u^2 + v^2)^{1/2} = 0.42$ cm s^{-1}, corresponds to vertical wavelengths of $55 < 1/m < 180$ m. This bandwidth corresponds to the low-wavenumber portion of the parametric representation (9), and thus the current-meter observations can be used to constrain the low-wavenumber power law r. The Doppler shifted spectrum is simply (Garrett and Munk 1972)

$$E(\omega) = \frac{1}{U}\int_k^\infty \frac{E(K_h)}{(K_h^2 - k^2)^{1/2}}\,dK_h, \tag{10}$$

where $f = 6.4 \times 10^{-5}$ s^{-1}, $N = 4.3 \times 10^{-3}$ s^{-1}, $B_{r0} = \sqrt{1.6}$, $U = 0.020$ m s^{-1}, and the energy spectrum is represented as E. A reasonable fit of (9) to the observations is obtained for $r = 2.0$ (Fig. 6).

Assuming an aspect ratio independent of vertical wavenumber, integration of (9) returns an rms vortical mode velocity of 0.7 cm s^{-1}. Notably, the total observed subinertial current was $(u^2 + v^2)^{1/2} = 2.2$ cm s^{-1}, so that this value of r returns an estimate of vortical mode kinetic energy consistent with Wunsch's (1997) assessment that 60%–70% of the depth-integrated, subinertial kinetic energy is contained in the lowest modes.

7. Summary and discussion

Observations of shear and strain spectra from midlatitudes were presented. We found

- shear/strain ratios for midlatitude data approached values between 1.5 and 2.0 at high wavenumber, in contrast to low-wavenumber values ranging over 5–11;
- S^2 and N^2 variability are increasingly correlated with decreasing vertical scale.

These signatures are consistent with a relative increase of low-aspect-ratio, vortical mode energy at small vertical scales. Vortical mode spectra were then inferred with the use of a quasi-permanent density finestructure model for the observed correlation between S^2 and N^2 in HRP data. The vortical mode spectrum was refined with the use of closely spaced current-meter records. The two data sources are complimentary. The correlation analysis is not a sensitive diagnostic of vortical mode energy at vertical wavelengths much larger than 50 m because the differentiation property of the least squares operator renders the estimates to be approximately local in the wavenumber domain. On the other hand, 10-m, vertical-wavelength vortical modes are buried in the superinertial signal of the current-meter records. Taken together, the HRP data constrain the high-wavenumber end of the vortical mode strain spectrum and the current-meter data constrain the low-wavenumber end.

A parametric representation of the vortical mode spectrum was proposed:

$$F_{z0} = \frac{Am_2^2 m^r}{(m_1^r + m^r)(m_2^2 + m^2)}, \qquad S_{z0} = 1.6\overline{N^2}F_{z0}.$$

Model constants return reasonable agreement with the data for $A = 3.15$, $m_1 = 0.055$, $m_2 = 0.155$, $r = 2.0$, and $S_{z0}/\overline{N^2}F_{z0} = 1.6$. The shear/strain ratio, or aspect ratio (3) in the low Ro limit, is assumed to be independent of vertical scale and set by the current-meter observations for vertical wavelengths $55 \leq \lambda_v \leq 180$ m. The inference of shear/strain ratio and B_{r0} at vertical wavelengths $\lambda_v \leq 30$ m is therefore tentative.

Assuming that the vortical mode aspect ratio and shear/strain ratio are independent of vertical scale, the vorticity Rossby number $\mathrm{Ro} = (\zeta/f) = B_{r0}[mS_{z0}(m)/\overline{N^2}]^{1/2}$, increases toward smaller scales but is less than 0.25 for $\lambda_v \geq 30$ m (Fig. 9). The inferred vortical mode field is linear and thus is best described as quasigeostrophic ($\mathrm{Ro} \ll 1$, $B_{r0}^2 \gg \mathrm{Ro}$) for these larger scales.

Assuming that the vortical mode aspect ratio and shear/strain ratio are independent of vertical scale, the resulting internal wave shear/strain and aspect ratios are largely independent of wavenumber for $0.01 \leq m \leq$ 0.1 cpm (Fig. 9). The increase of internal wave aspect ratio for $m \geq 0.1$ cpm may be associated with the presence of shear instabilities characterized by low shear/strain ratios, as that increase occurs on scales for which $\overline{S^2} \geq 1.0\overline{N^2}$, Fig. 3 and section 4. Alternately, the increasing internal wave strain spectrum (Fig. 5) could be a signature of increasing noise in the salinity calculation. Measurements of the shear/strain ratio from a nearly neutrally-buoyant float ranged from 2–4 for sensor separations of 5 m to 3–9 for sensor separations of 1 m (Fig. 2 of Kunze et al. 1990). These are in the range shown in Fig. 9. However, they suggest increasing shear/strain ratios with wavenumber in the range 0.1–0.5 cpm in contrast to the decreasing ratio with wavenumber in Fig. 9. Kunze et al. interpreted their results as indicating a dominance of finescale near-inertial waves at these scales, but note the difference in sampling stategies.

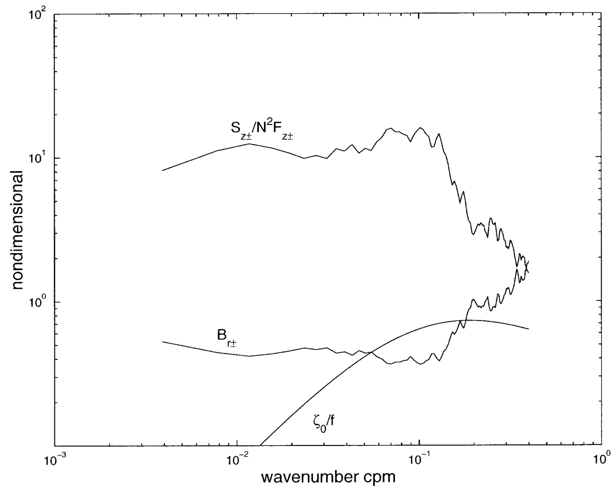

FIG. 9. Internal wave shear/strain ratio and aspect ratio for the NATRE HRP data and rms horizontal gradient of the vortical mode spectrum.

That shear/strain ratios should asymptotically approach relatively constant values at high wavenumber (Fig. 3) suggests a dynamical process. Implicit in the permanent density fine structure model (section 5) is an assumption that the amplitude of the internal wavefield varies according to the buoyancy-scaling defined by the WKB approximation. For a single internal wave, the WKB approximation implies, as well, a modulation of vertical wavenumber according to $m \cong m_o\overline{N}/N_o$, where m_o is a reference vertical wavenumber. A dynamical description of the interaction between internal waves and low-aspect-ratio vortical modes may well by characterized by this simple buoyancy scaling.

This coupling implies no energy exchange between internal waves and vortical modes. This coupling could, however, play a role in determining the relative spectral levels if a high-wavenumber diabatic sink (e.g., shear instability) drained energy from the waves during excursions to high wavenumber and the amplitude of the excursions was related to the vortical mode spectral level.

A related mechanism that does permit an adiabatic energy exchange is internal wave propagation in geostrophic shear. The coupling is well studied in the low Ro limit in which wave amplitudes and spatial scales are much smaller than those of the vortical modes (e.g., Bretherton and Garrett 1969). In this limit the energy exchange is simply the wave stress working against the geostrophic shear. Here, however, a near-equivalence between wave and vortical mode spatial scales appears appropriate and wave amplitudes are typically much larger. We are not aware of a similar characterization of energy exchanges for this parameter regime. It is more common for the energy exchanges to be viewed in terms of triads rather than propagation models [see Riley and Lelong (2000) for a recent review and references to the fast manifold/slow manifold debate].

A second dynamical perspective is provided by an equipartition statement. Given the linearized shear/strain (HKE/APE) ratios [(2) and (3)] and assuming the aspect ratios and energy densities of all three solutions are identical,

$$B_r = B_{r+} = B_{r-} = B_{r0}$$
$$S_{z+}(m) + \overline{N^2}F_{z+}(m) = S_{z-}(m) + \overline{N^2}F_{z-}(m) = S_{z0}(m) + \overline{N^2}F_{z0}(m),$$

it can be shown that

$$\frac{\sum [S_{z+}(m) + S_{z-}(m) + S_{z0}(m)]}{\sum [\overline{N^2}F_{z+}(m) + \overline{N^2}F_{z-}(m) + \overline{N^2}F_{z0}(m)]} = 2.0. \quad (11)$$

This simple result implies that under equipartition the total shear/strain ratio is constant, independent of aspect ratio B_r provided that the aspect ratios of the three normal-mode solutions are identical. The observed shear/strain ratios at high wavenumber are nearly equal to this value of 2.0. This result depends upon assuming the thermal wind relation for vortical modes. A reviewer notes that it is independent of vertical symmetry in the wavefield as long as the sum of the wave variance is twice the vortical mode variance. Equipartitioning within the internal wavefield is typically observed at $m \geq m_c$ and can be attributed to internal wave dynamics alone (Polzin 2002, manuscript submitted to *J. Phys. Oceanogr.*).

We mention this result (11) primarily because of its startling simplicity. We do not have a robust picture of how internal wave–vortical mode interactions would affect observed spectral amplitudes. We speculate that the simple buoyancy-scaling mentioned above may represent the required coupling between internal waves and vortical modes for this partitioning mechanism.

As potential-vorticity-carrying perturbations, vortical modes can only be created or destroyed through irreversible processes (Ertel 1942; Haynes and McIntyre 1987). At 400–800 dbar, the NATRE measurements analyzed here are isolated in space from topography and in time from the water mass formation regions for North Atlantic Central Water (10–20 years: Robbins and Jenkins 1998). The nearest topography is Great Meteor Seamount, which is located 250 km to the north of the survey grid. With prevailing flow to the southwest (Armi and Stommel 1983), products of topographic mixing are unlikely to be carried into the central part of the NATRE survey. Sufficient time has elapsed since these waters were subducted for finescale potential-vorticity anomalies created by atmospheric forcing to have been turbulently eroded. For a vertical diffusivity of $K_v = 1 \times 10^{-5}$ m^2 s^{-1}, buoyancy anomalies with 200-m vertical wavelengths would diffuse away in 3 years. Since the potential temperature–salinity relation at these depths is tight, thermohaline interleaving as a product of double diffusion is also an unlikely contributor.

While potential vorticity anomalies might be present as part of the potential enstrophy cascade in geostrophic turbulence, the m^{-1} gradient spectra that characterizes this regime (Charney 1971) is not found at vertical wavelengths $\lambda_z > 10$ m (Fig. 5). Efforts to explain the observed frequency spectrum (Fig. 6) as a cascade of enstrophy from Eulerian periods >10 days to periods <1 day will necessarily be quite convoluted if the spectral levels are required to match those of the vortical mode spectrum with the observed HKE/APE ratio. A simple frozen fine structure model such as (10) will not work. If the enstrophy cascade is discounted, what source maintains the vortical modes?

In the absence of viable external mechanisms, we consider the generation of buoyancy and potential vorticity anomalies by local irreversible mixing in isolated turbulence patches. An isolated mixing patch conserves potential vorticity integrated over a volumetric domain larger than the patch itself. Local anomalies, however, are created (Haynes and McIntyre 1987). While regions of static instability typically have vertical scales much smaller than 1 m, the turbulent patches have scales larger than those of statically unstable events. Such patches are apparent in the NATRE data and have vertical extents as large as the dominant vertical wavelength in the vortical mode gradient spectra [$2\pi/m_1$, (9)]. An example appears in Polzin (1996). We consider internal wave breaking to be a plausible source for the inferred vortical mode field.

The low-wavenumber, power law dependence of the proposed spectrum, $r = 2.0$, is inconsistent with that associated with an inverse energy cascade, for which $E(m) \propto m^{-5/3}$ and $r = 1/3$ for $m < m_1$. Metais et al. (1994) report numerical simulations of forced stratified rotating turbulence in which the inverse cascade is absent, and Bartello (2000) argues that a strong inverse cascade is possible for this geophysically relevant case only if the forward cascade (to smaller scales) is artificially inhibited. Our observations do not support an inverse cascade.

Considerable variability in both the generation and subsequent evolution of vortical modes is possible. The NATRE data likely represent typical midocean conditions with a background (near GM) internal wave state, a weak mesoscale eddy field, and little water mass variability. Other measurements have tentatively identified topographically generated vortical modes in the wake of a seamount (Kunze and Sanford 1993), in the very weak internal wavefield of the Beaufort Sea (D'Asaro and Morehead 1991) and generated by deep convection in the Labrador Sea (Lilly and Rhines 2002). More observations are required to define the climatological variability.

Acknowledgments. Constructive criticism from Steve Anderson greatly improved the assessment of the S^2–N^2 correlation. Gregg Holloway emphasized the notion that the three solutions to the f-plane equations be considered as independent dynamical modes, which then sparked the result (11). The authors gratefully acknowledge the support of NSF and ONR for the acquisition and analysis of these data. Final proofreading and editing was done by Anne-Marie Michael.

APPENDIX

A Wave Straining Model

Kunze et al. (1990) suggested that high-frequency, internal wave strain would affect near-inertial, internal wave shear as

$$\partial(v_{z2})/\partial t = -v_{z2}\partial(w_1)/\partial z, \qquad \text{(A1)}$$

where v_{z2} denotes the near-inertial shear and $w_1 = \eta_{1t}$ the high-frequency vertical velocity. Equation (A1) can be expressed as $\partial[\ln(v_{z2})]/\partial t = -\partial(\eta_{1z})/\partial t$, which has the solution $v_{z2}/v_{z0} = \exp(-\eta_{1z})$, where v_{z0} is the shear of wave 2 in the absence of straining by wave 1. Physically, this balance suggests that high-frequency straining produces exponentially larger changes of shear so that regions of higher-than-average stratification are regions of lower-than-average Richardson number, Ri $= N^2/S^2$. The resulting correlation between N^2 and S^2 is modeled assuming shear-squared and buoyancy-frequency-squared of the form

$$N_*^2 = (1 - \hat{\eta}_z)\overline{N^2}^{xyt}/\overline{N^2}$$
$$S_*^2 = \hat{S}^2 \exp(-2\hat{\eta}_z)\overline{N^2}^{xyt}/\overline{N^2}, \qquad \text{(A2)}$$

where $\hat{S}^2$ and $\hat{\eta}_z$ are uncorrelated random variables. After normalizing N_*^2 and S_*^2 by $\overline{N^2}/\overline{N^2}^{xyt}$, the correlation coefficient (8) reduces to

$$C(\Delta z) = \frac{\overline{S_*^2 N^2 \hat{\eta}_z e^{-2\hat{\eta}_z}}/\overline{e^{-2\hat{\eta}_z}}}{(\overline{S_*^4} - \overline{S_*^2}^2)^{1/2}(\overline{N_*^4} - \overline{N_*^2}^2)^{1/2}}. \qquad \text{(A3)}$$

The model correlation coefficient was estimated by evaluating (A3) directly from the NATRE data (Fig. A1). The model overpredicts the observed correlation by a considerable margin, particularly at large Δz. We conclude that, although high-frequency strain may play some role in modulating low-frequency shear and conspire to result in the observed correlation, (A1) does not explain the observed correlation.

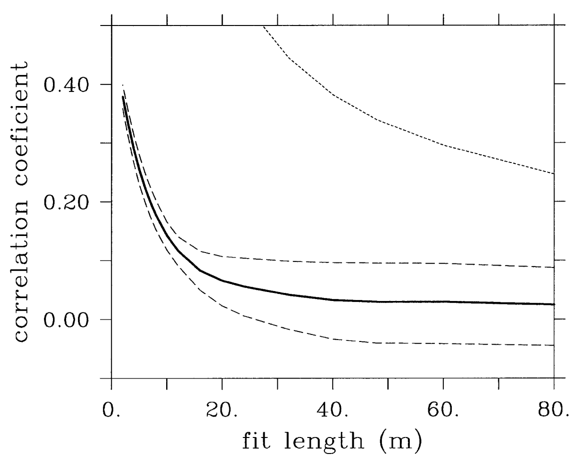

FIG. A1. Estimates of the S^2–N^2 correlation (7) as a function of fit length Δz. Thick lines represent data from 400 to 800 dbar. Dotted lines represent the rms variability in correlation coefficients that were estimated by dividing the data into 50-m depth bins. The thin solid line is a theoretical estimate using the wave-straining model (A1–A3).

REFERENCES

Anderson, S. P., 1992: Shear, strain and thermohaline fine structure in the upper ocean. Ph.D. thesis, University of California at San Diego, 173 pp.

Armi, L., and H. Stommel, 1983: Four views of a portion of the North Atlantic subtropical gyre. *J. Phys. Oceanogr.,* **13,** 828–857.

Bartello, P., 2000: Potential vorticity, resonance and dissipation in rotating convective turbulence. *Geophysical and Astrophysical Convection,* P. Fox and R. Kerr, Eds., Gordon and Breach, 275–287.

Bray, N. A., and N. P. Fofonoff, 1981: Available potential energy for MODE eddies. *J. Phys. Oceanogr.,* **11,** 30–46.

Bretherton, F. P., and C. J. R. Garrett, 1969: Wavetrains in inhomogeneous moving media. *Proc. Roy. Soc. London,* **302A,** 529–554.

Brink, K. H., 1995: Tidal and lower frequency currents above Fieberling Guyot. *J. Geophys. Res.,* **100,** 10 817–10 832.

Briscoe, M. G., 1977: On current finestructure and moored current-meter measurements of internal waves. *Deep-Sea Res.,* **24,** 1121–1131.

Cairns, J. L., and G. O. Williams, 1976: Internal wave observations from a mid-water float, 2. *J. Geophys. Res.,* **81,** 1943–1950.

Charney, J. G., 1971: Geostrophic turbulence. *J. Atmos. Sci.,* **28,** 1087–1095.

D'Asaro, E. A., and M. D. Morehead, 1991: Internal waves and velocity finestructure in the Arctic Ocean. *J. Geophys. Res.,* **96,** 12 725–12 738.

——, and R. C. Lien, 2000: Lagrangian measurements of waves and turbulence in stratified flows. *J. Phys. Oceanogr.,* **30,** 641–655.

Desaubies, Y., and W. K. Smith, 1982: Statistics of Richardson number and instability in oceanic internal waves. *J. Phys. Oceanogr.,* **12,** 1245–1259.

Duda, T. F., and C. S. Cox, 1989: Vertical wavenumber spectra of velocity and shear at small internal wave scales. *J. Geophys. Res.,* **94,** 939–950.

Eriksen, C. C., 1978: Measurements and models of fine structure, internal gravity waves, and wave breaking in the deep ocean. *J. Geophys. Res.,* **83,** 2989–3009.

Ertel, H., 1942: Ein neuer hydrodynamischer Wirbelsatz. *Meteorol. Z.,* **59,** 277–281.

Garrett, C., and W. Munk, 1971: Internal wave spectra in the presence of fine-structure. *J. Phys. Oceanogr.,* **1,** 196–202.

——, and ——, 1972: Space–time scales of internal waves. *Geophys. Fluid Dyn.,* **2,** 225–264.

——, and ——, 1975: Space–time scales of internal waves: A progress report. *J. Geophys. Res.,* **80,** 291–297.

——, and ——, 1979: Internal waves in the ocean. *Ann. Rev. Fluid Mech.,* **11,** 339–369.

Hayes, S. P., H. B. Milburn, and E. F. Ford, 1984: TOPS: A free-fall velocity and CTD profiler. *J. Atmos. Oceanic Technol.,* **1,** 220–236.

Haynes, P. H., and M. E. McIntyre, 1987: On the evolution of vorticity and potential vorticity in the presence of diabatic heating and friction or other forces. *J. Atmos. Sci.,* **44,** 828–841.

Henyey, F. S., J. Wright, and S. M. Flatté, 1986: Energy and action flow through the internal wave field: An eikonal approach. *J. Geophys. Res.,* **91,** 8487–8495.

Holloway, G., 1983: A conjecture relating oceanic internal waves and small-scale processes. *Atmos.–Oceans,* **21,** 107–122.

Horne, E. P. W., and J. M. Toole, 1980: Sensor response mismatches and lag correction techniques for temperature-salinity profilers. *J. Phys. Oceanogr.,* **10,** 1122–1130.

Howard, L. N., 1961: Note on a paper of John W. Miles. *J. Fluid Mech.,* **10,** 509–512.

Kunze, E., 1985: Near-inertial wave propagation in geostrophic shear. *J. Phys. Oceanogr.,* **15,** 544–565.

——, 1993: Sub-mesoscale dynamics near a seamount. Part II: The partition of energy between internal waves and geostrophy. *J. Phys. Oceanogr.,* **23,** 2589–2601.

——, and T. B. Sanford, 1993: Submesoscale dynamics near a seamount. Part I: Measurements of Ertel vorticity. *J. Phys. Oceanogr.,* **23,** 2567–2588.

——, and J. M. Toole, 1997: Tidally driven vorticity, diurnal shear and turbulence atop Fieberling Guyot. *J. Phys. Oceanogr.,* **27,** 2663–2693.

——, A. J. Williams III, and M. G. Briscoe, 1990: Interpreting shear and strain finestructure from a neutrally buoyant float. *J. Geophys. Res.,* **95,** 18 111–18 126.

——, R. W. Schmitt, and J. M. Toole, 1995: The energy balance in a warm-core ring's near-inertial critical layer. *J. Phys. Oceanogr.,* **25,** 942–957.

Ledwell, J. R., A. J. Watson, and C. S. Law, 1998: Mixing of a tracer in the pycnocline. *J. Geophys. Res.,* **103,** 21 499–21 529.

Lien, R., and P. Müller, 1992: Consistency relations for gravity and vortical modes in the ocean. *Deep-Sea Res.,* **39,** 1595–1612.

Lilly, J. M., and P. B. Rhines, 2002: Coherent eddies in the Labrador Sea observed from a mooring. *J. Phys. Oceanogr.,* **32,** 585–598.

McComas, C. H., and F. P. Bretherton, 1977: Resonant interaction of oceanic internal waves. *J. Geophys. Res.,* **82,** 1397–1412.

——, and P. Müller, 1981: The dynamic balance of internal waves. *J. Phys. Oceanogr.,* **11,** 970–986.

Metais, O., J. J. Riley, and M. Lesieur, 1994: Numerical simulations of stably-stratified rotating turbulence. *Stably-Stratified Flows—Flow and Dispersion over Topography,* I. P. Castro et al., Eds., Clarendon, 139–151.

Miles, J. W., 1961: On the stability of heterogeneous shear flows. *J. Fluid Mech.,* **10,** 496–508.

Müller, P., 1984: Small-scale vortical motions. *Internal Gravity Waves and Small-Scale Turbulence: Proc. 'Aha Huliko'a Hawaiian Winter Workshop,* Honolulu, Hawaii, University of Hawaii at Manoa, 249–262.

——, D. J. Olbers, and J. Willebrand, 1978: The IWEX spectrum. *J. Geophys. Res.,* **83,** 479–500.

Polzin, K. L., 1992: Observations of turbulence, internal waves and background flows: An inquiry into the relationships between scales of motion. Ph.D. thesis, MIT/WHOI, 244 pp.

——, 1996: Statistics of the Richardson number: Mixing models and finestructure. *J. Phys. Oceanogr.,* **26,** 1409–1425.

——, J. M. Toole, and R. W. Schmitt, 1995: Finescale parameterizations of turbulent dissipation. *J. Phys. Oceanogr.,* **25,** 306–328.

Riley, J. J., and M.-P. Lelong 2000: Fluid motions in the presence of strong stable stratification. *Ann. Rev. Fluid Mech.,* **32,** 613–658.

Robbins, P. E., and W. J. Jenkins, 1998: Observations of temporal changes of Tritium–^{3}He age in the Eastern North Atlantic thermocline: Evidence for changes in ventilation? *J. Mar. Res.,* **56,** 1125–1161.

Roden, G. I., 1991: Mesoscale flow and thermohaline structure around Fieberling Seamount. *J. Geophys. Res.,* **96,** 16 653–16 672.

Rossby, T., 1988: Five drifters in a Mediterranean salt lens. *Deep-Sea Res.,* **35,** 1653–1663.

Rubenstein, D. M., and G. O. Roberts, 1986: Scattering of inertial waves by an ocean front. *J. Phys. Oceanogr.,* **16,** 121–131.

Schmitt, R. W., J. M. Toole, R. L. Koehler, E. C. Mellinger, and K. W. Doherty, 1988: The development of a fine- and microstructure profiler. *J. Atmos. Oceanic Technol.,* **5,** 484–500.

Sherman, J. T., and R. Pinkel, 1991: Estimates of the vertical wavenumber-frequency spectra of vertical shear and strain. *J. Phys. Oceanogr.,* **21,** 292–303.

St. Laurent, L., and R. W. Schmitt, 1999: The contribution of salt fingers to vertical mixing in the North Atlantic Tracer Release Experiment. *J. Phys. Oceanogr.,* **29,** 1404–1424.

Toole, J. M., R. W. Schmitt, K. L. Polzin, and E. Kunze, 1997: Near-boundary mixing above the flanks of a mid-latitude seamount. *J. Geophys. Res.,* **102,** 947–959.

Weller, R. A., D. L. Rudnick, C. C. Eriksen, K. L. Polzin, N. S. Oakey, J. M. Toole, R. W. Schmitt, and R. T. Pollard, 1991: Forced ocean response during the Frontal Air–Sea Interaction Experiment. *J. Geophys. Res.,* **96,** 8611–8638.

Wunsch, C., 1997: The vertical partition of oceanic horizontal kinetic energy. *J. Phys. Oceanogr.,* **27,** 1770–1794.